Estimating Permeability in Shales and Other Heterogeneous Porous Media: Deterministic vs. Stochastic Investigations

Maria Apostolopoulou[1], Ron Dusterhoft[2], Richard Day[3], Michail Stamatakis[1], Marc-Olivier Coppens[1], and Alberto Striolo[1,*]

[1] Department of Chemical Engineering, University College London, Torrington Place, London, WC1E 7JE

[2] Halliburton, 3000 N Sam Houston Pkwy E, Houston, Texas 77032, USA

[3] Halliburton, Building 4, Chiswick Park 566, London W4 5YE, United Kingdom

* Corresponding author: a.striolo@ucl.ac.uk

Abstract

With increasing global energy demands, unconventional formations, such as shale rocks, are becoming an important source of natural gas. Extensive efforts focus on understanding the complex behavior of fluids (including their transport in the sub-surface) to maximize natural gas yields. Shale rocks are mudstones made up of organic and inorganic constituents of varying pore sizes (1-500nm). With cutting-edge imaging technologies, detailed structural and chemical description of shale rocks can be obtained at different length scales. Using this knowledge to assess macroscopic properties, such as fluid permeability, remains challenging. Direct experimental measurements of permeability supply answers, but at elevated costs of time and resources. To complement these, computer simulations are widely available; however, they employ significant approximations, and a reliable methodology to estimate permeability in heterogeneous pore networks remains elusive. For this study, permeability predictions obtained by implementing two deterministic methods and one stochastic approach, using a kinetic Monte Carlo algorithm, are compared. This analysis focuses on the effects resulting from pore size distribution, the impact of micro- and macropores, and the effects of anisotropy (induced or naturally occurring) on the predicted matrix permeability. While considering multiple case studies, recommendations are provided on the optimal conditions under which each method can be used. Finally, a stochastic analysis is performed to estimate the permeability of an Eagle Ford shale sample using the kinetic Monte Carlo algorithm. Successful comparisons against experimental data demonstrate the appeal of the stochastic approach.

Keywords: kinetic Monte Carlo; Effective Medium Theory; Simplified Renormalization; anisotropy; shale formations

1 Introduction

Global primary energy consumption has been increasing, slowly but steadily, during recent years—1% during 2016, 0.9% during 2015, 1% during 2014—compared to a 10-year average yearly increase of 1.8%.[1] To meet these energy demands, in addition to developing renewable energy sources, the focus is on optimizing the processes to recover hydrocarbons from the subsurface.[2] For instance, shale gas has gained significant attention, and industrial breakthroughs have contributed to reducing production costs.[3] Nevertheless, our understanding of fluid transport within heterogeneous rocks typically identified in shale formations remains limited because of the rocks' complex texture.[4] Experimentally measured properties of shale rocks (i.e., porosity, chemical composition, pore size distribution (PSD), and wettability) vary greatly.[5] Estimating the permeability of porous media will not only assist toward improved production rates but will also minimize potential risks associated with the technologies currently implemented to stimulate shale formations. Predicting reliably medium permeability requires (1) selecting the appropriate transport model to quantify the physical properties that microscopically dictate fluid transport and (2) implementing effective methods to predict the system's macroscopic behavior. While many physical properties for shale samples have been reported (PSD, mineralogy, organic content), not much progress has been made on combining these datasets to yield useful information regarding permeability.

Understanding the behavior of fluid transfer through porous rock formations, in particular permeability, has been in the spotlight for many years.[6,7] Cutting-edge imaging techniques provide detailed structural and chemical analysis of materials at different length scales,[8] but incorporating this knowledge systematically into models that can predict macroscopic properties remains challenging. Experimental methods can supply the necessary information, but are often costly, time consuming, or even impractical.[9] On the contrary, computer simulations are cost effective, but are often limited in terms of accuracy or availability of computational resources;[10] therefore, a compromise among the levels of detail needed, the accuracy expected, and the computational cost should be determined. For this work, we implement and compare three approaches to predict permeability of complex pore networks representing those identified in shale rocks. Two of the methods are deterministic, and one is stochastic. It is important to highlight that all computational approaches can fail to predict the overall permeability of highly heterogeneous systems, compared to experiments, because of the uncertainty associated with the exact value of the properties assigned to each domain, as well as with uncertainties related to the extent and connectivity of the three-dimensional (3D) pore network.

The first efforts in predicting the effective permeability, given the permeability of the pores present in the medium, were reported half a century ago,[11] with Renard and Marsily describing and assessing the available techniques at the time.[12] Among multiple deterministic methods, the Effective Medium Theory (EMT)[13–16] was determined suitable for (1) media exhibiting small heterogeneities with low variance and a log-normal permeability distribution, and (2) binary media containing less than 50% low-permeability pores.[12] The implementation of EMT is straightforward and computationally efficient. As a result, the EMT method has been applied in many different fields, including geological formations and sediments, composite media, heterogeneous catalysts and mixed-matrix membranes with fillers.[17–21] It is generally accepted that when the low-permeability proportion exceeds a certain threshold (i.e., 50%), EMT yields poor predictions.[12,21] It has been suggested that this low performance is because of the overestimation of the network connectivity.[20,22] While recent findings have helped improve our understanding regarding both the percolation threshold and the mechanisms responsible for poor EMT performance,[23] a robust EMT approach with an evident identification of its limits of applicability is still elusive.

Another deterministic approach often used for estimating equivalent media permeability, particularly by the oil and gas industry, is King's renormalization approach.[24] For this approach, one begins from a grid in a dimensional space (DS), constructed by considering 2^n cells per coordinate, yielding 2^{nDS} meshes. Aggregations are performed iteratively, with each iteration combining two cells per coordinate, thereby producing a less finely discretized grid, with $2^{(n-1)DS}$ meshes. The procedure is completed when one single mesh emerges.[12] As part of King's renormalization approach, an electric network was used as analogous to a porous medium in which the inverse of permeability acts as a resistance.[24] Le Loc'h proposed a simplified renormalization technique that performs successive

groupings between the meshes. If two meshes are in series relative to flow direction, point permeabilities are averaged using a harmonic mean. If the two meshes are in parallel with respect to flow, an arithmetic mean is used instead. The two approaches yield minimum and maximum permeability, respectively. The equivalent permeability is estimated as the geometric mean of these extremes.[25] Kelkar recommended this approach as a reservoir characterization strategy, and Naraghi et al. implemented it to calculate the permeability of an Eagle Ford sample.[26,27] Renormalization techniques share EMT weaknesses when applied to systems with high heterogeneity, where highly permeable regions neighbor with low-permeable ones.[24] Shale rock samples are indeed heterogeneous materials; thus the mentioned deterministic approaches might not be reliable tools to predict the effective rock permeability.

Stochastic approaches have been developed to assess the permeability of complex heterogeneous systems.[12] Such approaches capture the variability and complexity of permeability-controlling parameters, such as the porosity, PSD, and network connectivity. Among other stochastic approaches, Renard and Marsily identified Monte Carlo (MC) methods capable of quantifying the uncertainty of the permeability distribution. They suggested that a successful approach should implement a two-part workflow: (1) individual 'local' permeabilities should be stochastically generated and (2) deterministic techniques should be applied to scale up the model and simulate fluid flow through the complex pore network.[12] It should be evident that kinetic MC (KMC) approaches require significant computational resources, and their performance strongly depends on how well the pore network structure is known.

A typical MC algorithm samples over a probability distribution, and randomly selects properties.[28] Alternatively, KMC can follow molecular trajectories and yield permeability calculations with satisfactory accuracy and orders of magnitude lower computational cost compared to Molecular Dynamics (MD) simulations.[29,30,31]

The promise of fast and straightforward estimates makes deterministic approaches appealing to practitioners. However, considering the nature of shale formations (high heterogeneity and a significantly large percent of micro-porosity due to the contribution of small pores[32]) the deterministic approaches considered here may be inapplicable. For this work, we aim to test the applicability of the EMT and the simplified renormalization technique in shales. We compare our findings against predictions based on our version of the stochastic KMC algorithm. We use synthetic pore networks to identify those characteristics that may greatly affect permeability. The synthetic pore networks are also used to perform a sensitivity analysis, which could be useful to identify which method to implement for studying a given rock sample. When using synthetic pore networks, our analysis focuses on pore size and network connectivity; we consider pore sizes that follow log-normal distributions and assume that 'local' permeability coefficients depend solely on pore size. Further, we consider networks with low, medium and high anisotropy; estimate media permeability; and use the same pore mapping to evaluate the three methods and identify applicability ranges of each approach, using a detailed understanding of the physical mechanisms responsible for the differences observed. Finally, we assess the applicability of the three methods on an actual shale sample. Emphasis is placed on the applicability of the KMC approach to predict the permeability of a shale rock sample and the results are used to critically comment on the assumptions commonly made to characterize such materials. Our results suggest that, due to the complex pore networks found in shales, and given the uncertainty regarding whether a specific sample is representative of the reservoir overall behavior, stochastic approaches such as the KMC model implemented here are recommendable.

The remainder of this paper is organized as follows: Section 2 provides the mathematical formulation of the three methods and describes the simulation set-up used. Section 3 describes the methodology, Section 4 discusses the results, starting from the validation of an algorithm applied to the KMC method implemented here, and then comparing permeability predictions from the three methods implemented here. Section 5 highlights conclusions and recommendations regarding the implementation of the three methods. The systematic use of synthetic networks allows us to critically evaluate the applicability of the three methods.

2 Methods

2.1 EMT

The EMT approach is indicated as 'Method I' in what follows.

For this work we use Kirkpatrick's formalism, which was introduced to evaluate the electric conductivity of a network of conducting elements. This formalism is adapted to calculate the equivalent permeability for a lattice-based pore network, which is treated as a site percolation problem. In our approach, illustrated in Fig. 1, $k_{i,j}$ is the permeability coefficient of a site and k_{eff} is the effective matrix permeability, which is calculated via Eq. (1). More information on the derivation of Eq. (1) can be found in the Supplementary Material.

$$\sum_{j=1}^{N_C}\sum_{i=1}^{N_R} \varphi_{i,j}\frac{k_{eff}-k_{i,j}}{\left[\left(z/2-1\right)\right]k_{eff}+k_{i,j}} = 0 \qquad (1)$$

In Eq. (1), N_R is the number of matrix rows, N_C is the number of columns. The coordination number z is kept constant and equal to 4,[33] as we consider rectangular two-dimensional (2D) networks. Building on previous work on KMC,[29] the term "voxel" refers here to a single cell of a matrix representing a pore network. For Eq. (1), the frequency term $\varphi_{i,j}$ acts as a weighting factor on the permeability coefficient $k_{i,j}$. The weight of $\varphi_{i,j}$ represents the pore volume fraction represented by each voxel. In our matrices the voxels are considered to contain the same volume of pores, and hence all $\varphi_{i,j}$ have the same weight:

$$\varphi_{i,j} = \frac{1}{N_C \text{ x } N_R} \qquad (2)$$

2.2 Simplified Renormalization Method

The simplified renormalization method is indicated as 'Method II'. To calculate the effective rock permeability using Method II, we follow the description by Naraghi et al. for a 2D matrix:[27]

$$k_{UB} = \frac{N_R}{N_C}\frac{1}{\sum_{i=1}^{N_R}\frac{1}{\sum_{j=1}^{N_C}k_{i,j}}} \qquad (3)$$

$$k_{LB} = \frac{N_C}{N_R}\sum_{j=1}^{N_C}\frac{1}{\sum_{i=1}^{N_R}\frac{1}{k_{i,j}}} \qquad (4)$$

$$k_{eff} = \sqrt{k_{LB}k_{UB}} \qquad (5)$$

In Eqs. (3-5) $k_{i,j}$ is the permeability of the pores represented by voxel (i,j). According to these equations, the flow direction is vertical (top to bottom), and zero cross flow is imposed. Fig. 1 provides a schematic of the calculation of k_{LB} and k_{UB}.

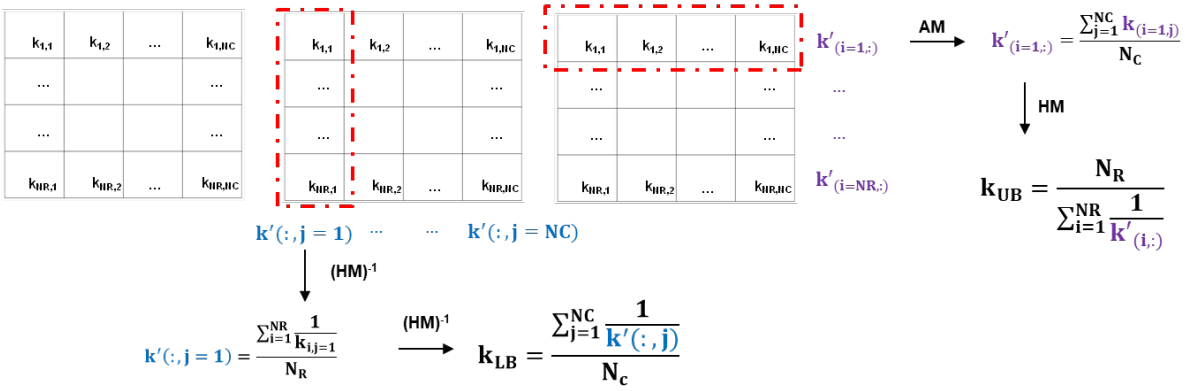

Fig. 1. Schematic of simplified renormalization Method algorithm; (left) matrix considered and the voxels' IDs; (middle) process for calculating k_{LB}; (right) process for calculating k_{UB}; AM stands for arithmetic mean and HM for harmonic mean. Eq. 5 is used to calculate the effective matrix permeability.

2.3 Stochastic KMC Approach

The KMC approach is indicated as 'Method III'. From a stochastic perspective, the tendency to move from the pores present in one voxel to those present in another is described by probabilities. Our KMC approach, applied to one-dimensional (1D) pore networks, is described by Apostolopoulou et al.[29] The underlying model of the KMC simulation is the Master Equation (Eq. 6), which can be thought of as a "probability balance". The Master Equation expresses the rate of change for the probability of finding the system in state p, in terms of the probability influx from other states q, and the probability efflux toward these other states:[34,35]

$$\frac{dP_p(t)}{dt} = -\sum_{q\neq p} W_{pq}P_p(t) + \sum_{q\neq p} W_{qp}P_q(t) \qquad (6)$$

The state vectors p and q in Eq. (6) capture the information necessary to describe the location of diffusing fluid particles in the porous network of interest. Thus, a state vector stores the number of particles contained in each and every voxel of the network. The generic Master Eq. (6) can be used to describe the diffusion of a particle from voxel i,j to voxel i,j+1 as follows: in state q, voxel i,j has $n_{i,j} - 1$ particles and voxel i,j+1 has $n_{i,j+1} + 1$ particles. Comparing Eq. (1) and Eqs. (3-6) shows W_{pq} to be a function of $k_{i,j}$ (refer to Eqs. (7-8) and Fig.2), which allows us to quantitatively compare the different methods.

KMC algorithms are designed to simulate stochastic realizations of the Master Equation.[36] For this work, we extend our previous 1D matrix-based KMC algorithm, which was applied to a two-phase system, to 2D. This extension causes an increase in the number of possible moves a particle can undertake. For our 1D model a particle can either move to the left or to the right voxel at each algorithmic step, while in our 2D approach a particle can access the voxels above and below its position, in addition to those on the left and on the right. In the 2D approach implemented here, we

only consider one-phase systems of methane at supercritical conditions (see Table 1). We implement the 2D KMC algorithm to monitor the populations of diffusing particles and assess the overall permeability of a rock sample. We also perform simulations whereby we monitor the location of a single diffusing particle within the matrix mesh, in order to assess anisotropy effects. Fig. 2 describes schematically the algorithmic steps implemented for our KMC approach. The Mersenne Twister MT19937 uniform random number generator was used to obtain sequences of random numbers.[37]

The computational efficiency of the KMC algorithm is strongly dependent on the matrix mesh as the computational cost to select each KMC step scales with the number of possible events. For a N × N matrix with z=4, there are 4 × N × N possible events at each step. Note that for implementing our 1D KMC model to a matrix consisting of N voxels, the number of possible events would be 2 × N, which is $^1/_{2N}$ fewer than those needed to implement the 2D KMC model. For a system with few voxels (i.e., N<50), the computational time required for conducting simulations within a 1D KMC model could extend to several seconds on a standard desk-top computer, while for an equivalent 2D model several minutes would be required. Other factors that challenge the computational efficiency of the KMC algorithm include the size of the system (number of particles) and the distribution of the KMC rates.[38] Considering that the latter factors depend on the investigated system, and hence can be rarely optimized, the computational efficiency of the KMC algorithm is usually improved by selecting an efficient event-selection algorithm. Event selection can be performed in a linear or branching manner, with the latter making use of binary tree representations of priority queues;[39] for efficiency purposes, we implemented the latter approach in our 2D KMC model. The validation of the branching method and the computational savings achieved are reported in Section 4.1.

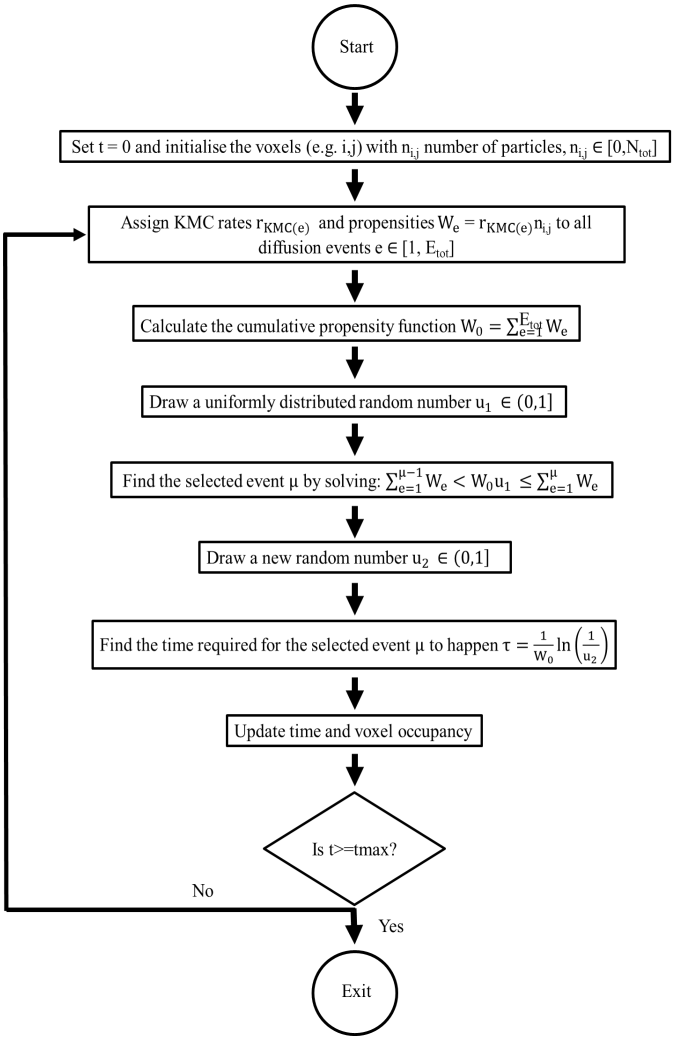

Fig. 2. Schematic of the KMC algorithm implemented in the study.

2.4 Selection of Parameters

To directly compare results obtained when Methods I, II, and III are implemented, we maintained all system properties constant, including permeability coefficients. This is straightforward when either the EMT or renormalization methods are implemented, because the permeability coefficients are parameters in Eq. (1) and Eqs. (3-5). When the KMC approach is implemented, the permeability coefficients, $k_{i,j}$, expressed in m^2 or Darcy for Methods I and II, should be translated into KMC rates, expressed in s^{-1}, to simulate stochastic realizations of Eq. (6). To this end, we combined Darcy's[40] and Fick's[41] law in the following relation between diffusion coefficients, $D_{i,j}$, in m^2/s and permeability:

$$D_{i,j} = \frac{k_{i,j}\Delta P}{\Delta C} \tag{7}$$

where ΔP is the pressure difference applied to the system and ΔC is the fluid concentration difference (see the following description). The validation of Eq. (7) is provided in Appendix A; supplementary data. To calculate KMC rates, we use:[30]

$$r_{KMC} = \frac{D_{i,j}}{\delta^2} \tag{8}$$

The KMC rate for each transition depends on the permeability coefficient of the neighbor/final destination. The assumption implicit in Eq. (8) is that the fluid transport from voxel to voxel takes place without encountering any thermodynamic barrier. For Eq. (8), $D_{i,j}$ is the diffusion coefficient as calculated using Eq. (7), and δ is the distance between the centers of two consecutive voxels. It is assumed that when a transition takes place, the effective distance covered by the particles equals δ. An example of the methodology followed to calculate the effective matrix permeability using Methods I, II, and III, is provided in Appendix A; supplementary data, where we further demonstrate that all three methods produce equivalent effective matrix permeability values when a homogeneous network is considered, thus suggesting that further manipulation of the results (e.g., within the Smooth Field Approximation)[42] is not necessary.

2.5 Simulation Setup

2D pore networks (matrices) are constructed, each containing N_C columns and N_R rows along the x- and y- axis. The voxels in the matrix are cubic. The transport within the system can only occur on the xy plane, because the thickness along the z-axis is assumed to be negligible for a narrow cylindrical pore. It is assumed that the particles within voxels are well mixed.

To estimate the effective matrix permeability using Methods I and II, permeability coefficients were assigned to each voxel, and Eq. (1) and Eqs. (3-5) were implemented, respectively. The assigned permeability coefficients were calculated based on the methodology proposed by Coppens[43] and Naraghi et al.:[27]

$$k_{i,j} = \frac{\eta M}{RT\rho_{av}}\frac{\theta}{\tau}(\delta'^{D_f-2})\, D_{k_{i,j}} + k_{D_{i,j}}\left(1 + \frac{b_{i,j}}{P}\right) \tag{9}$$

$$b_{i,j} = \left(\frac{8\pi RT}{M}\right)^{0.5} \frac{\eta}{R_{i,j}}\left(\frac{2}{\alpha_{i,j}} - 1\right) \quad (10)$$

$$\alpha_{i,j} = 1 - \log(1 + Kn_{i,j}{}^{0.7}) \quad (11)$$

$$D_{k_{i,j}} = \frac{2R_{i,j}}{3}\left(\frac{8RT}{\pi M}\right)^{0.5} \quad (12)$$

In Eqs. (9-12) η is the gas viscosity, M is the molar mass, R is the ideal gas constant, T is the temperature in Kelvin, ρ_{av} is the average gas density, θ is the rock porosity, τ is the tortuosity, $R_{i,j}$ is the pore radius of the voxel (i,j), D_f is the fractal dimension of the pore surface, Kn is the Knudsen number, D_k is the Knudsen diffusion coefficient in a smooth cylindrical pore, k_D is the Darcy permeability, and δ' is the ratio of normalized molecular size to local average pore diameter. Here, it is assumed that the pores are smooth, so that $D_f = 2$; this would have to be adjusted for fractal pores. Once the properties of the diffusing gas are calculated, the diffusion coefficient is determined solely from the pore diameter.

In our model, we assume physical properties that represent supercritical methane, as summarized in Table 1, together with rock characteristics. Note that the critical temperature of methane is 190.6 K at 4.6 MPa.[44] The rock total organic content (TOC) shows the % volume of the organic matter and is used to construct the shale network (see Section 3.4). Initially, a number of particles corresponding to a methane concentration C, are placed at the top of the matrix, while the rest of the system is empty. We maintain the particle concentration C at the top of the matrix constant at all times during our calculations. The amount of particles needed for the simulations is determined by knowing the voxels' volume and the methane density. Since the KMC matrix requires an area in which the particle concentration is constant, we add a row above the top row of the matrix. As this is a computational requirement for implementing the KMC model, the properties of this row are not taken into consideration when implementing Methods I and II.

The left and right matrix boundaries are reflective, while the bottom one is open: once the particles reach the bottom boundary, they can either exit the matrix or move to other neighboring voxels. Because of the initial configuration selected, the particles on average move through the matrix along the vertical direction, from the top to the bottom boundary. A counter is used to track the number of particles leaving the matrix from the bottom boundary during the simulation. Once a particle leaves the matrix, it is deleted from the simulation. Effectively, this particle can be thought of as entering a large empty voxel at the bottom of the domain. To set this up in the KMC simulation an 'absorbing' row is added to the bottom of the matrix. The properties of this absorbing row are not used for Methods I and II.

Table 1: Input parameters used for the permeability simulations for all three methods.

Parameter	Value
CH_4 Temperature (T)	300 K
CH_4 Pressure (P)	10 MPa
CH_4 Concentration (C)	4685.9 mol/m^3
Rock Porosity (θ)	10%
Rock Tortuosity (τ)	2
Rock volumetric (TOC)	12%

As described by Apostolopoulou et al.,[29] we maintain a constant pressure and concentration difference during the simulation. To analyze the results, we monitor the number of particles leaving the domain ΔQ at constant time steps Δt. The time step selected depends on the configuration used, described in Section 3. The slope of the linear fits is used to calculate the molecular flux J:

$$J = \frac{\Delta Q}{\Delta t \, A \, N_A} \tag{13}$$

In Eq. (13), A is the cross-sectional area available for the particles to leave the matrix. The matrix effective permeability (Method III) is calculated using Darcy's law:

$$k_{eff} = -\frac{J \Delta x}{\Delta P} \tag{14}$$

In Eq. (14), Δx is the matrix length, disregarding the top and bottom rows, added for computational requirements. The pressure drop is obtained by subtracting the pressure at the bottom (0 MPa) from the pressure at the top of the matrix (10 MPa). For our approach, it is assumed that the macroscopic flow follows Darcy's law, while allowing for Knudsen diffusion to occur within voxels containing narrow smooth pores, as described in Eqs. (9-12).

3 Systems Investigated

3.1 Model Networks to Test Sensitivity to Pore Size Distribution

The general consensus is that deterministic methods, such as Methods I and II, provide accurate predictions when the properties investigated follow a narrow log-normal distribution. Such distribution is described by the probability density function $P(x) = \frac{1}{\sigma\sqrt{2\pi}} e^{-(\ln x - \mu)^2 / 2\sigma^2}$, where x is a log-normally distributed random variable, μ is the mean and σ is the standard deviation of the variable's logarithm. Thus, we assume a log-normal distribution (μ, σ^2) of pore sizes. The distribution's μ is kept constant (μ = 37.5 nm or μ = 1.57 on the logarithmic scale), but σ varies between 0.1 and 1 on the logarithmic scale (Fig. 3). While increasing σ, the proportion of micropores (0-2 nm), mesopores (2-50 nm) and macropores (>50 nm)[45] changes. Pore classification follows IUPAC guidelines.[45]

Methods I, II, and III were used to predict the effective medium permeability. We generate 10 pore networks for each σ value. Note that this number (10) is selected as it is small, and therefore requires reasonable computational resources, but sufficient to ensure that the permeability values calculated for the various σ scenarios have confidence intervals that do not overlap, even when a 99.9% confidence level is selected (see Appendix A; supplementary data). Because Method III is stochastic, we perform 10 independent KMC simulation runs for each pore network. Note that completing one KMC simulation run requires significant computing time (several minutes), while deterministic methods require only a few seconds on a modern desktop computer. A 10 x 10 matrix was used for each σ value considered and the voxels used to create the matrix had dimensions 100 x 100 x 1 nm. Using a 10 x 10 matrix is advantageous, considering the computational time required, but can sometimes generate networks that are not representative, because of the reduced size of the lattice. To ensure that all networks simulated were representative, we plotted the PSD of each potential network generated against the target PSD. Those lattices that deviated from the target were rejected. This was a necessary process in our implementation.

A stochastic algorithm assigned pore sizes to the matrix voxels, according to the PSD selected, and Eq. (9) was used to assign the permeability to each voxel. Since the number of stochastic realizations generated is small (10) we implemented Monte Carlo (MC) sampling over the PSDs to generate stochastic realizations, as suggested by Naraghi et al.[27] However, to generate a larger number of stochastic realizations, more computationally efficient algorithms should be implemented. For example, the First-Order Reliability Approach (FORM) can produce realizations similar to those obtained with MC sampling, but significantly faster.[46,47] Another way to produce stochastic realizations is via geostatistical simulations, a method widely used in the petroleum industry to characterize heterogeneous reservoirs that allows generation of many equally probable realizations, which can then be post-processed to quantify and assess uncertainty. For instance, Karacan et al. implemented sequential Gaussian simulation (SGSIM) and sequential Gaussian co-simulation (co-SGSIM) techniques to generate stochastic realizations of coal.[48] We implemented a previously reported stochastic MC sampling technique, to generate our 2D pore networks,[27,49,50] and we also used a stochastic method (Method III) to simulate the fluid transport of the gas particles (KMC) through the generated pore networks. The time step used for the KMC sampling was set at 100 ns (see Appendix A; supplementary data for further details). Once all simulations are completed, we average the effective permeabilities calculated $\langle k_{eff}(\sigma)\rangle$ for each σ value, report these values for comparison against results from Methods I and II, and estimate the error bars for KMC calculations using:

$$\text{Error} = \frac{\text{STD}(k_{eff}(\sigma))}{\sqrt{n}} \qquad (15)$$

In Eq. (15), $\text{STD}(k_{eff}(\sigma))$ is the standard deviation of the values obtained in each individual KMC run for a given PSD, and n is the number of observations (10 for the simulations previously discussed).

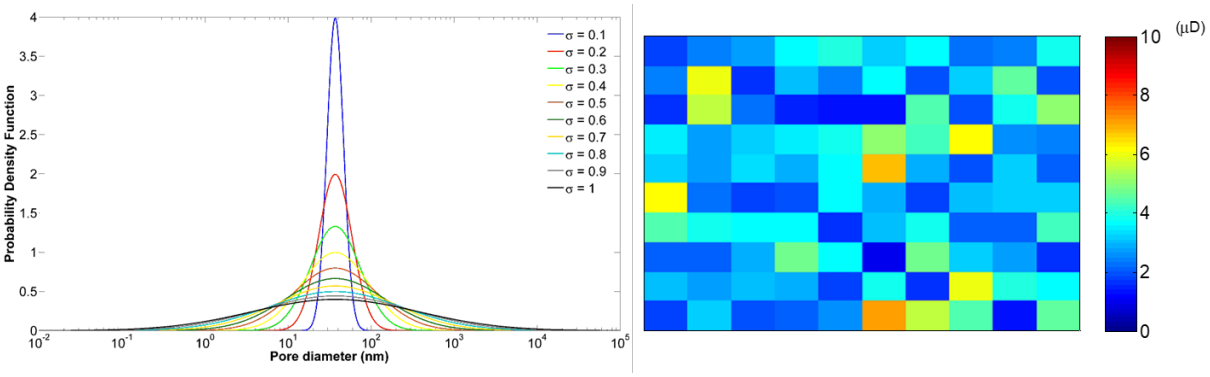

Fig. 3. (Left): Log-scale PSDs considered in our analysis. In all cases the distribution's μ is 37.15 nm or μ = 1.57 on the logarithmic scale, while σ ranges between 0.1 and 1 (on the logarithmic scale). (Right): Example of spatial arrangement of the permeability coefficients for σ =0.1.

3.2 Model Networks to Test Sensitivity to Micro- and Macropores

It is commonly accepted that Methods I and II provide satisfactory predictions when the proportion of low-permeability pores is low, in general < 50%, and the system is sufficiently far from the percolation threshold. To assess how the differences among predictions obtained by implementing Methods I, II, and III change as the proportion of low-permeability pores varies, we generate three pore-networks in which the volume proportion of low-permeability pores is 25%, 50% and 75%, respectively. Note that, in our simplification, each voxel is assumed to contain an equal pore volume, and that all the pores within a voxel are considered to be of the same size. In other words, each voxel represents a region containing only micro-, meso-, or macropores. Each voxel contains different numbers of perfectly conducting pores resulting in an equal pore volume per voxel.

The pore networks considered in this sub-section are dual-permeability systems, generated within two scenarios: (1) a system comprising only micropores and mesopores; or (2) a system of mesopores

and macropores. The micropores considered have a 1 nm diameter, yielding a permeability coefficient of 15 nD (note that the pore size determines the permeability, according to Eq. 9). Mesopores and macropores were assumed to have diameters of 10 nm and 100 nm, respectively. The corresponding permeability coefficients are 0.3 μD and 17 μD and the dual permeability 10 x 10 matrix networks consisted of 100 voxels, each with dimensions of 500 x 500 x 1 nm.

Fig. 4 shows the networks generated; note that in the pore networks of Fig. 4 there is no distribution of pore diameters: there are only three possible values for these diameters, capturing micro-, meso- or macropores. Panels a, b, and c show the spatial arrangement of the micro- and mesopores for 25%, 50% and 75% micropores, respectively; panels d, e, and f show the arrangement of macro- and mesopores. The KMC sampling step was 5 ns and 50 ns for systems (1) and (2), respectively.

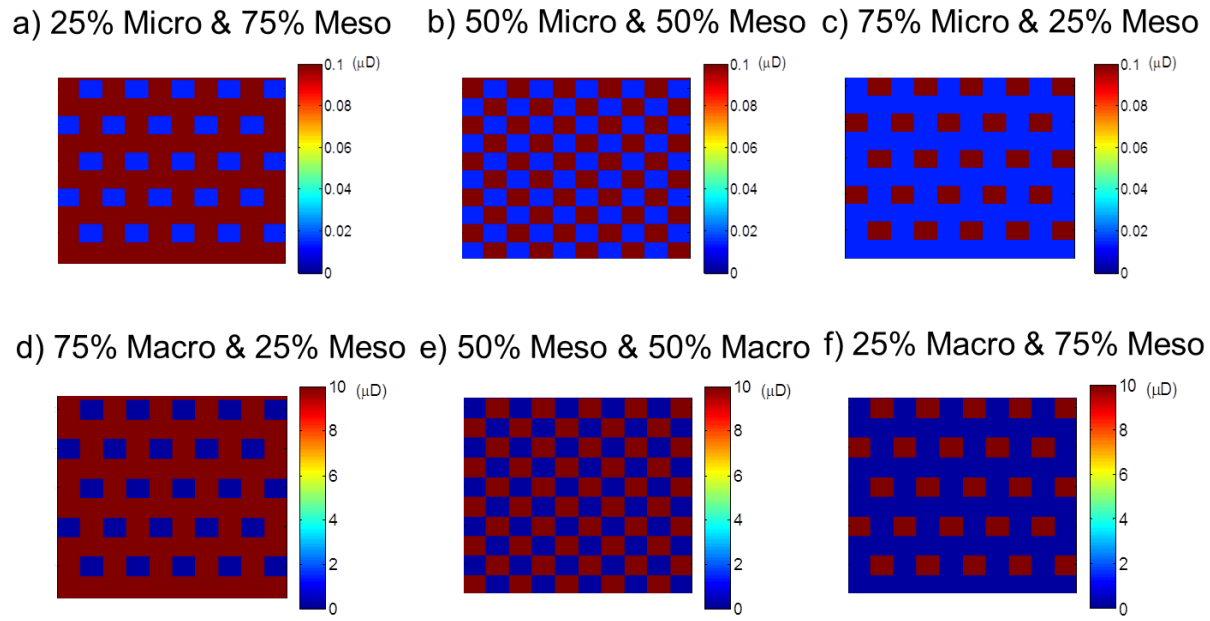

Fig. 4. Networks consisting of micro- and mesopores (a-c) and macro- and mesopores (d-f). The color bars show the permeability coefficients assigned, in μD.

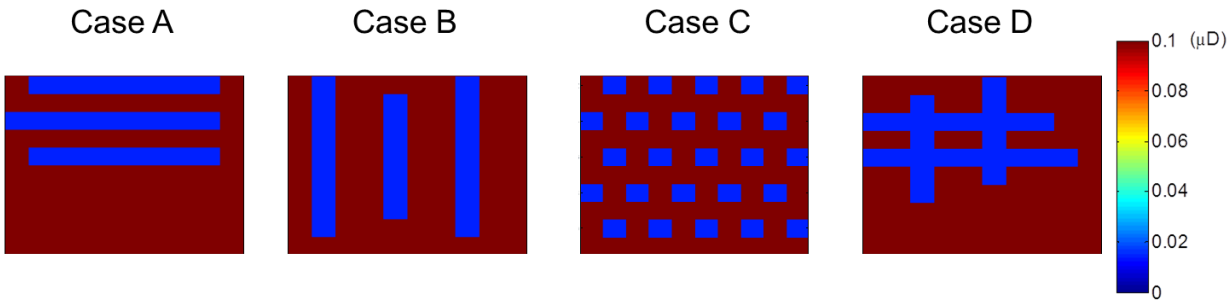

Fig. 5. Dual-permeability networks with different anisotropic distributions. Cases A and B exhibit high anisotropy and cases C and D have low and moderate anisotropy. The color bars show permeability coefficients in μD.

3.3 Model Networks to Test Sensitivity to Anisotropic Distributions

Methods I and II are expected to face difficulties in differentiating between isotropic or anisotropic distribution of pores within a network, while it is likely that the stochastic KMC approach has the ability to differentiate between permeability along different directions within an anisotropic network. In shale

rock samples, evidence confirms that permeability is indeed anisotropic.[51] To quantify the sensitivity of the methods considered here to the anisotropic distribution of pores, we create dual-permeability matrices in which the proportion of the low and high-permeability voxels is kept constant (25% and 75%, respectively), but these components are spatially distributed in four different configurations (Fig. 5). Fig. 5 shows that the low-permeability values are aligned (A) horizontally; (B) vertically; (C) in a grid; and (D) both horizontally and vertically. The low and high-permeability pores are characterized by 15 nD and 0.3 μD permeability coefficients, respectively. For each configuration, we conducted 3 independent KMC simulation runs. The matrix size used for all four cases was 10 x 10, the voxel dimensions were 500 x 500 x 1 nm, and the sampling time step was 5 ns (see Appendix A; supplementary data for further details).

We quantified the anisotropy of each system by implementing Principal Component Analysis (PCA), as described by Ringnér and Bui et al.[52,53] The unit cells considered for the PCA had periodic boundary conditions in all directions, and when the particle crossed a boundary, its new position was equal to the position in the unit cell plus the unit cell vector along the direction of the crossing. The initial position of the particle was randomized 100 times. The particle was not allowed to start from the same initial position more than once. From each initial position, we performed 200 independent runs; hence, we performed 20,000 independent runs for each configuration. We obtained the position of a single particle after 50 ns and the final position of the particle on the x and y direction was plotted against its initial origin.

Based on obtained trajectories, we calculated the covariance matrix, along with its eigenvectors and eigenvalues. The eigenvectors revealed the direction of the principal axis while the eigenvalues established the degree of variance for the data in that direction. The differences observed in the estimated eigenvalues are indicative of the degree of anisotropy. Additionally, we calculated the diffusion coefficient in the x and y directions, and in the xy plane by considering a single methane particle, and we followed its trajectory for a total of 5 μs to obtain its mean square displacement (MSD). We calculated D_x, D_y and D_{xy} coefficients using Einstein's relation, on the basis of the calculated MSDs:

$$\mathrm{D_x} = \frac{1}{2}\lim_{\mathrm{t}\to\infty}\frac{\langle|\mathrm{x_i(t)} - \mathrm{x_i(0)}|^2\rangle}{\mathrm{t}} \tag{16}$$

$$\mathrm{D_y} = \frac{1}{2}\lim_{\mathrm{t}\to\infty}\frac{\langle|\mathrm{y_i(t)} - \mathrm{y_i(0)}|^2\rangle}{\mathrm{t}} \tag{17}$$

$$\mathrm{D_{xy}} = \frac{1}{4}\lim_{\mathrm{t}\to\infty}\frac{\langle|\mathbf{r_i(t)} - \mathbf{r_i(0)}|^2\rangle}{\mathrm{t}} \tag{18}$$

In Eqs. (16-18), $\langle|\mathrm{r_i(t)} - \mathrm{r_i(0)}|^2\rangle$ is the MSD in the xy-plane and $\mathbf{r_i(t)} = (\mathrm{x_i(t)}, \mathrm{y_i(t)})$. PCA and diffusivity analyses were performed using KMC.

3.4 Experimental Shale Sample

We considered a realistic pore network, based on an experimental sample. Naraghi et al.[27] applied King's simplified renormalization method on the scanning electron microscope (SEM) image of an Eagle Ford shale sample (Fig. 6). Light grey areas represent inorganic components, and dark grey represents organic components. Naraghi et al.[27] segmented the image and determined the probability distribution of the organic block's size, referred to as "patch size" in their work. The patch size distribution is a normal, Gaussian distribution with a mean of 5 μm and a standard deviation of 1 μm.

To assign permeability coefficients within organic and inorganic components, Naraghi et al. used PSD data obtained from Brunauer, Emmett, and Teller (BET) measurements. They assumed that organic and inorganic components follow distinct log-normal PSDs and reported the distributions' means and standard deviations. We assume that the μ and σ of the distributions, expressed on the log-scale, are 0.63 and 0.18 for the organic component, and 1.57 and 0.44 for the inorganic matter, respectively. These values are slightly different compared to those reported by Naraghi et al. but produce PSDs that closely match those reported by the authors. Naraghi et al. first generated a model pore network by assigning organic and inorganic components and then distributed pore sizes within the two components, while sampling from the appropriate distribution. The permeability coefficients were calculated using Eq. (9), and the effective network permeability was estimated using Method II.

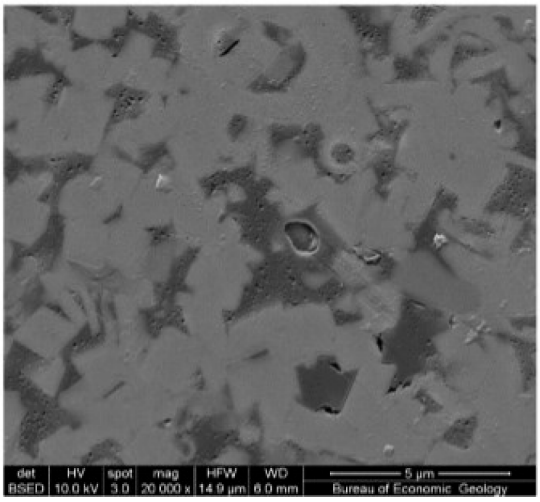

Fig. 6. SEM image of an Eagle Ford sample, reproduced from Ref. [27]. Dark grey regions correspond to organic matter and light grey to inorganic matter.

We considered the experimental SEM image of Fig. 6 in our study, to calculate the effective matrix permeability using Methods I, II, and III, but also generated additional networks following the approach by Naraghi et al. to distribute organic patches within the inorganic matter for our model matrix. We used the volumetric TOC to condition the total amount of organic pores assigned within our models and we assigned pore sizes within the organic and inorganic matter according to the reported distribution properties. In our approach, we separately calculated the effective matrix permeability of the organic and inorganic matter to reduce the computational load of the KMC simulations; similar calculations were not necessary using Model I and II.

To calculate the effective organic and inorganic permeability, we generated 10 matrices consisting of 10 x 10 voxels in each case with voxel dimensions of 20 x 20 x 1 nm and 350 x 350 x 1 nm for the organic and inorganic matter, respectively. We calculated the effective permeability mean and error bars from all three methods for both components and we then used these 'effective' organic and inorganic permeability values to construct the dual permeability network, which represents the rock of Fig. 6. To calculate the permeability of the dual permeability network, we considered a 15 x 15 matrix consisting of 1 μm x 1 μm x 1 nm voxels.

To consistently compare Methods I, II, and III to calculate the network's effective permeability, we used the organic and inorganic permeabilities obtained from the previous step as input. The KMC sampling time step was 1 ns for all calculations (organic, inorganic, dual-permeability), and we performed 10 independent KMC runs for each dual-permeability configuration. Using the KMC method, we also calculated the confidence interval to achieve 99.9% confidence level to ensure that using 10 stochastic realizations for organic, inorganic, and network permeability yields meaningful conclusions, especially when the KMC data are compared against experiments.

4 Results and Discussion

4.1 Validation of the Branching Algorithm

At each step of the KMC simulation, an event is selected and executed, resulting in the occupancy at each voxel changing while the simulation progresses; as a consequence, the propensities need to be updated over time as the KMC simulation progresses (propensity is defined as the product of the KMC rate and occupancy at each voxel). For a classic KMC algorithm (linear event selection), after each event execution, the list of all propensities is scanned and updated. Simulating progressively larger systems results in a sharp increase of the computation time required by this algorithm. Yet, because in our protocol only one particle transitions at each simulation step, not all propensities change after the execution of an event. Thus, to save computing time, we implemented a branching algorithm, which identifies the voxels affected by the event being executed, and it updates only the propensities associated with these voxels. For systems consisting of many voxels (>50), implementing the branching algorithm results in significant computational savings. To test and validate the branching algorithm implemented, we generated a 100×100 2D uniform lattice with permeability 0.1 μD.

Using the same sequence of random numbers, we execute the KMC algorithm twice – the first time, the selection of transition events taking place each time follows the schematic in Fig. 2 (we refer to this approach as the linear search or “classic” algorithm); the second time, we apply the branching algorithm. Then, we report the ID of the event selected in both cases and compare the events to determine if the event selected is the same in both simulations. We assign a value of “0” when there is agreement between the two algorithms and a value of “1” whenever a different event is being selected. For the 3,000 events sampled, there was always agreement between the events selected using the two different algorithms, as the value obtained was always “0”.

To quantify the computational savings achieved by implementing the branching vs. the classic algorithm, we monitored the CPU time necessary to identify and execute the event at each step. In Fig. 7 we compare the CPU time necessary for the branching algorithm in red, and the one for the classic algorithm in blue. Visual analysis confirms that the computational demand is smaller when the branching algorithm is implemented compared to that necessary using the linear search algorithm.

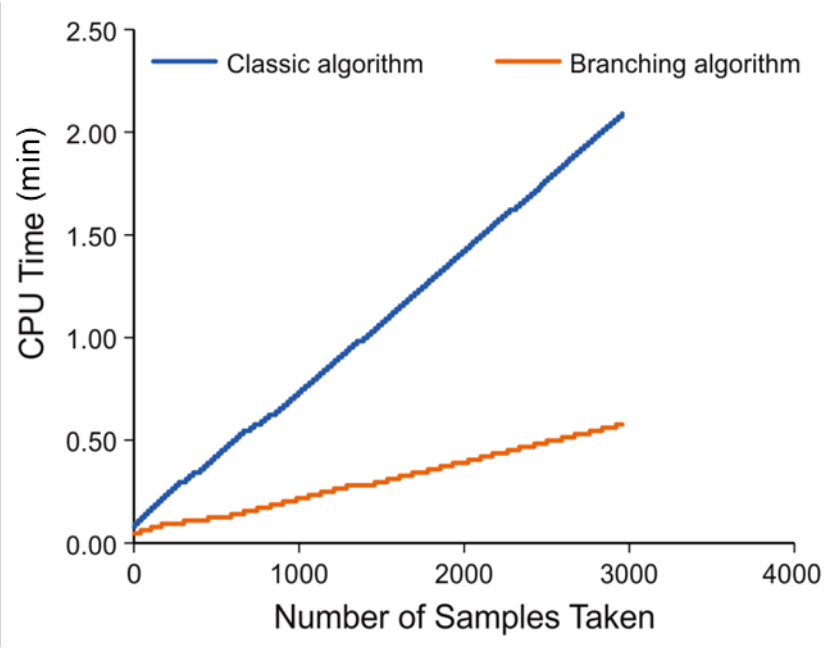

Fig. 7. Computational savings when implementing the branching vs. classic algorithm in a KMC simulation conducted in a 100×100 lattice.

4.2 Pore Size Distribution Effects

Fig. 3 shows that for the log-normal PSDs considered, in which the mean was kept constant, as σ increased, the amount of both micro- and macropores present in the sample increased. We monitored the proportion of the micro-, meso- and macropores for the different σ values, and computed the effective matrix permeability for each distribution using Methods I, II, and III. Fig. 8 shows the results; A) shows the absolute results from the three approaches in terms of matrix effective permeability; B) shows the percent deviation of the deterministic Models I and II compared to the stochastic calculation (Model III); and C) shows the analysis of the PSD in terms of % structural composition due to micro-, meso-, and macropores.

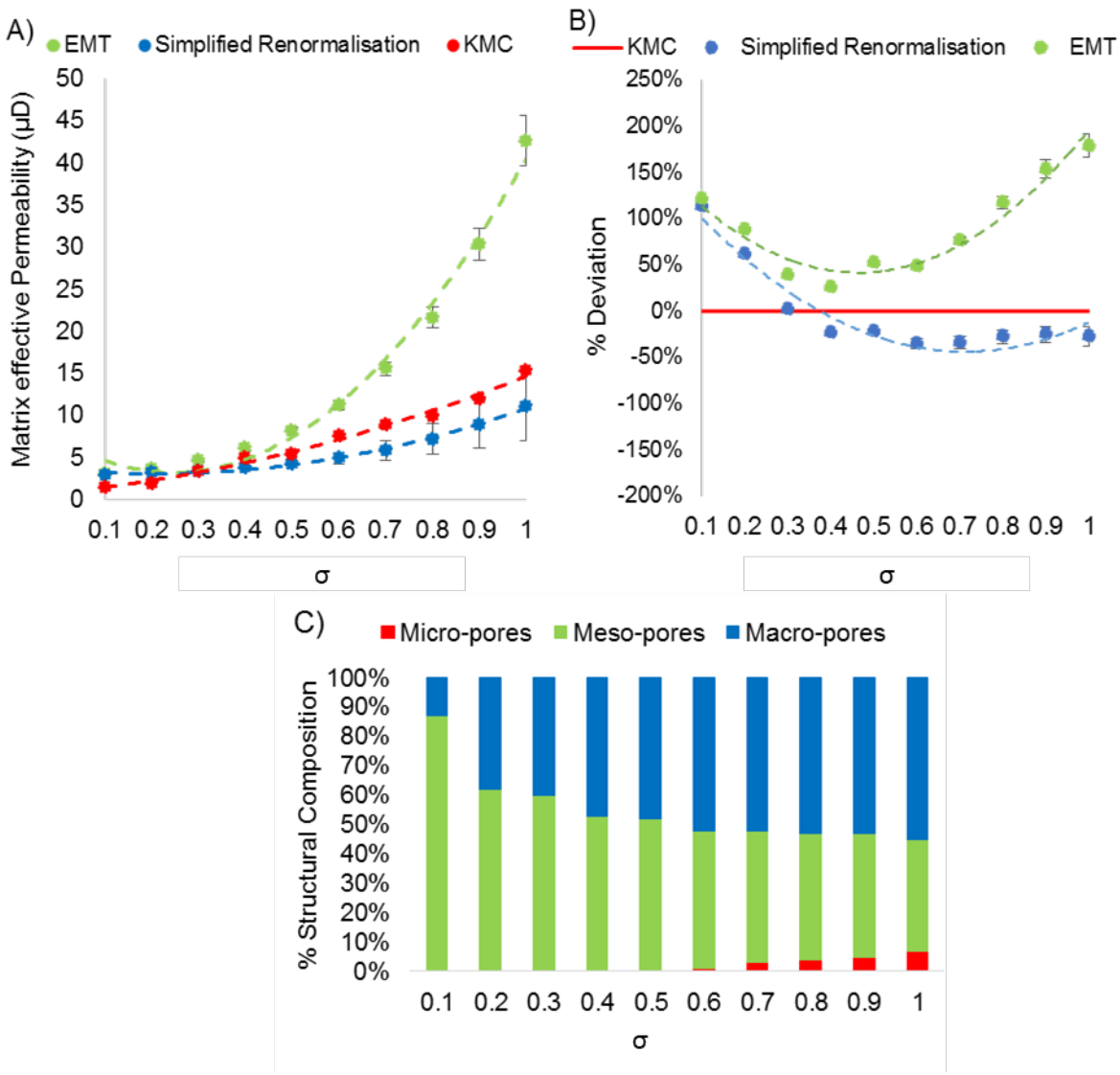

Fig. 8. (A) Comparison of the three methods used in this study as a function of the distribution's σ; KMC error bars are estimated to be smaller than the size of the marker. (B) Percent deviation of the deterministic models compared to the stochastic calculation. (C) Percent of volume comprised of micro-, meso- and macropores in each system shown in (A). Lines in (A) and (B) are guides to the eye. The matrices simulated here are isotropic with PSDs shown in Fig. 3.

When σ ranged between 0.1 and 0.2, the majority of the pore volume consisted of mesopores, yielding an isotropic network with a high proportion of low-permeability pore volume (only macropores are considered to be high-permeability pores in our analysis). Both deterministic methods overestimated the effective network permeability, compared to the KMC. This result agrees with expectations based on literature, because the high-permeability component (macropores) represents a low number fraction of the respective pore networks, and the deterministic Models I and II are expected to over-estimate the contribution of high-permeability pores under the conditions tested.

When σ ranged between 0.3 and 0.4, there was good agreement among all three methods. Fig. 8C shows that the volume fraction of macropores in the samples continuously increased as σ increased; for σ greater than 0.4, such pores accounted for the majority of pore volume in the system. At these conditions, the deterministic methods are expected to be accurate, and indeed our results show small deviations compared to predictions based on the stochastic KMC approach, reinforcing these

observations reinforce our hypothesis that the stochastic KMC method can yield accurate predictions for effective medium permeability.

When σ=0.5, the pore network still contained only meso- and macropores; however, there were 1% fewer mesopores (by volume) and 1% more macropores compared to the network characterized by σ=0.4. In this scenario, our results demonstrate that Method I (EMT) significantly over-estimated the permeability, compared to both Methods II and Method III, suggesting that the EMT approach is highly sensitive to the presence of high-permeability components. Further, both Methods II and III predicted increases in effective permeability, because of the increased amount of macropores in the system, but the effect was moderate.

When σ ranged from 0.6 to 1.0, the pore networks contained significant amounts of micro-, meso- and macropores. For σ=0.6, micropores accounted for 1% (by volume) of the pores in the network and macropores for 52% (by volume). Method I predicted rapid increases in the effective permeability as σ increased, which increasingly diverged from the KMC predictions, confirming the high sensitivity of EMT to high-permeability pores in the network. Method II yielded effective permeability predictions that were lower compared to those obtained by the KMC algorithm. Actually, we observed that for PSDs with σ>0.3, Method III (KMC) predicted an effective permeability between those predicted by Method I and by Method II. This is due to the EMT's sensitivity to macropores and to the zero cross-flow assumption implicit in Eqs. (3-5), which describe Method II.

For distributions with σ between 0.7 and 1, the volume fraction of mesopores dropped, while the volume fraction of micro- and macropores increased. The EMT continued to predict very high effective matrix permeability, while the simplified renormalization (Method II) yielded a permeability lower than that obtained using Method III. The effective permeability predicted by Method I was up to ~10 times larger than that predicted by Method II, based on our case study. Even though the volume of micropores present in the network increased when σ>0.7, both Methods II and III predicted an increased permeability as σ increased. This is because, as the distributions of the pores in the networks became broader, the generated networks contained larger macropore volumes as well.

4.3 Micro- vs. Macropore Effects

The preceding investigation exhibits the sensitivity of the EMT on macropores. To quantify the methods' sensitivity on micropores, we performed a sensitivity analysis for all three methods using dual-permeability networks consisting of micro- and mesopores, and meso- and macropores, respectively (Fig. 4). We report our findings in Fig. 9, in which A) and B) depict the effect of micro- and macropores to the effective matrix permeability, respectively.

We started with quantifying the effect of micropores (A). When 25% of the pore volume consisted of micropores and the rest were mesopores, KMC and EMT methods yielded effective permeabilities in excellent agreement with each other. This is expected, considering the amount of the relatively low-permeability component is low for these networks. It is perhaps surprising that Method II underestimated the effective matrix permeability by almost half. This is due to the assumption of zero cross-flow, which likely does not hold when the pore network of Fig. 4a, is considered, coupled with a pressure difference imposed along the top-bottom direction.

When the proportion of micropores in the volume increased from 25% to 50%, the network's connectivity was effectively reduced. As a result, the zero cross-flow assumption became acceptable, and Model II predicted an effective permeability that agreed well with what KMC predicted. All models yielded effective permeability values that were lower than those for the matrix with 25% micropore volume, which is expected. The fact that Methods II and III yielded predictions in excellent agreement with each other suggests that the KMC approach provides realistic estimates of the matrix permeability, since the network of interest had poor connectivity in the direction of flow. It is not surprising that Method I (EMT) over-estimated the effective permeability compared to the other two approaches, as EMT fails when the system is close to the percolation threshold. When the micropores account for 75% of the pores in the sample, by volume, Fig. 4c, both deterministic Methods I and II overestimated the effective matrix permeability.

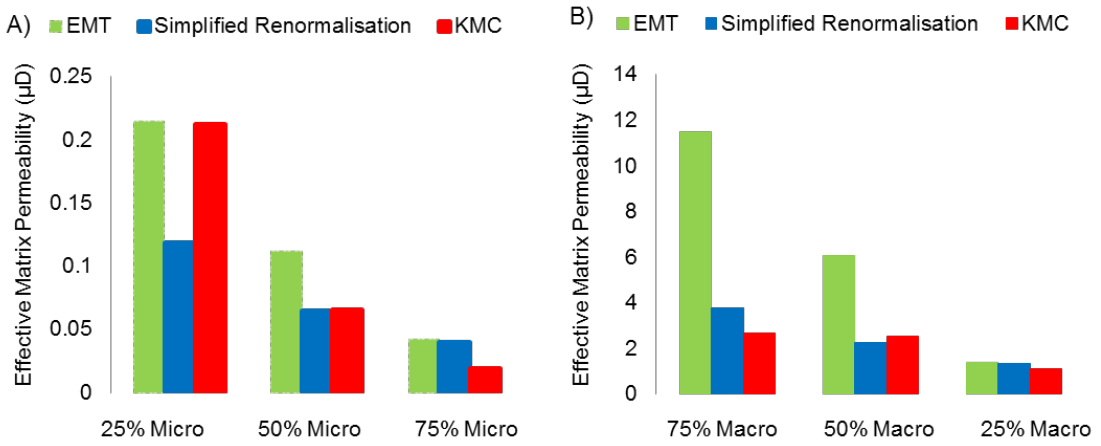

Fig. 9. Sensitivity analysis on the pore type in dual-permeability networks (Fig. 4) with varying component % by volume; (A) shows results for the network consisting of micro- and mesopores; (B) for the network with meso- and macropores.

Considering the effect of macropores (Fig. 4, d-f, pore networks), the results (Fig. 9B) suggest that there is satisfactory agreement between the predictions by Methods III (KMC) and II (simplified renormalization) for most of the cases. When 75% of the pore volume consisted of macropores, in the dual permeability network (Fig. 4d), both deterministic methods were highly sensitive to the presence of high-permeability pores, with Method I (EMT) significantly overestimating the effective permeability. The sensitivity of EMT to high-permeability coefficients was further evidenced by the extent of the over-prediction. When the % volume content of macropores was equal to that of mesopores, (Fig. 4e), the EMT method overestimated the permeability, while Methods II and III were in satisfactory agreement. More specifically, the KMC's prediction lies between the two analytical methods, validating our previous observation for σ 0.5 where the % of meso- and macropores was almost equivalent. The gap between the predictions of the EMT and the two other methods became smaller as the % of high-permeability components decreased. For 25% macropores (Fig. 4f), the deterministic methods provided a slightly overestimated value for the matrix's permeability. In that case, the KMC's prediction was lower because the 25% of macropores present in the system were not well connected. The same behavior was observed for the case of 25% micro- and 75% mesopores, where the deterministic methods predicted almost identical values, but higher than the KMC's estimation, validating the reliability of our KMC methodology, as it accounts for the network's connectivity.

4.4 Anisotropy Effects

The networks considered for the previous analysis probe the sensitivity of the three methods to micro- and macropores. In all pore networks considered so far (Fig. 3 and Fig. 4) pore sizes were distributed uniformly within the networks. To quantify the effect of anisotropic distribution of the pores, we considered dual-permeability networks containing 25% by volume micropores and 75% by volume mesopores. Four configurations were generated (Fig. 5 Cases A-D) and, in all of them, the flow direction was along the y-axis. We calculated the effective matrix permeability using Methods I, II, and III; Fig. 10 shows the results.

To further assess the effect of an anisotropic pore distribution, we calculated the diffusion coefficient of a particle representing a single methane molecule along the x and y directions, as well as its 2D diffusion coefficient in the xy plane (results in Fig. 10). In Fig. 11 we provide PCA results to test whether diffusion coefficients and measures of anisotropy can provide insights for the network's effective permeability.

The results in Fig. 10 show that Method I (EMT) did not capture the anisotropic distribution of the pores within the network. This is expected, considering that EMT neglects the detailed network structure. Method II (simplified renormalization) exhibited some effects, because of the connectivity of the pores in the network, but the predicted changes in the effective medium permeability can be considered negligible. These observations are in stark contrast with the results obtained by the stochastic Method III (KMC), which exhibited high sensitivity to the anisotropic distribution of the pores. The enhanced reliability of Method III is because KMC allows fluid transport to occur along both x and y directions.

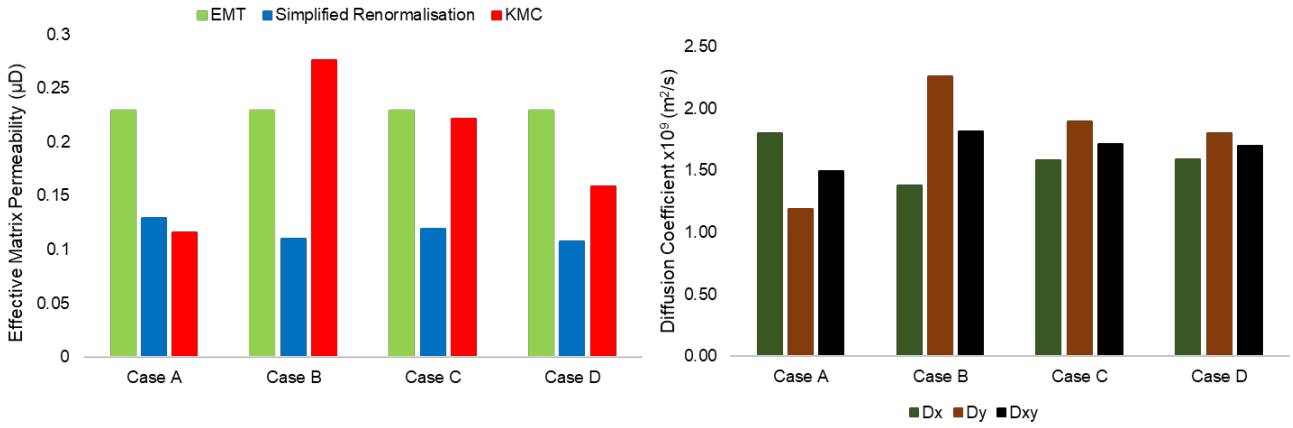

Fig. 10. Effective matrix permeability calculation using the three methods for networks with varying anisotropy (left) and diffusivity analysis in the x and y directions and the xy plane (right).

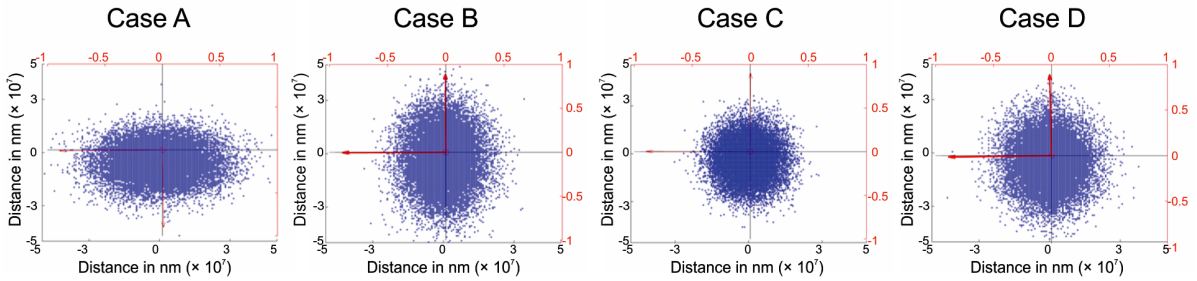

Fig. 11. PCA analysis of the anisotropic networks. The black x-axis shows the first principal component and the black y-axis the second. The red arrows are vectors showing the preferential diffusion direction.

For the (Fig. 5, Case B) pore network, the voxels containing the micropores were aligned in the y direction, resulting in Method II predicting lower permeability than that predicted by Method III. For the KMC simulation, the vertical bars formed by voxels containing micropores added a kinetic barrier to the system, resulting in the fluid particles diffusing through the network and physically “avoiding” the low-permeability pathways. Because the micropores were aligned along the flow direction, the fluid particles were not forced to pass through them, as opposed to the situation represented by the network presented in Case A where Methods II and III predicted similar permeability. Further, our results demonstrate that Methods I and III are in good agreement for Case C, which is expected, because the pore network considered in this representation is homogeneous. The lowest matrix permeability predicted with the KMC approach corresponds to the Case D network in Fig. 5. For this system, both x and y directions exhibited anisotropy; however, 2% by volume of mesopores were

surrounded by micropores, and therefore contributed little to the matrix effective permeability. While KMC was able to account for this effect, both Methods I and II failed to do so.

According to the diffusion coefficient calculated on the xy plane (see right panel of Fig. 10), the following trend was observed, exhibiting the diffusivity in descending order: Case B > C > D > A. For the diffusion coefficient calculated along the y direction, the same trend was observed. The effective matrix permeability calculated by the KMC method agrees with this order; however, note that considering the diffusion coefficients alone can lead to false predictions. For instance, the bars corresponding to Cases C and D in Fig. 10, right, were similar; however, the corresponding KMC-predicted matrix permeability significantly varied because of the isolated mesopores identified in Case D. PCA analysis was unable to capture this difference, as can be seen in Fig. 11. The results for Cases A and B highlight the anisotropy on the x and y direction, respectively, while Cases C and D resemble almost isotropic patterns. These observations were confirmed by the molecular trajectories and the % differences for the eigenvalues (Fig. 11) were calculated to be 51%, 64%, 16% and 13% for cases A, B, C, and D, respectively. It is evident that both diffusivity coefficients and PCA analysis are not able to predict the low network connectivity represented by Case D.

It should be pointed out that predictions obtained by Methods I and II could be improved, especially when they are applied to anisotropic networks, by implementing specifically-derived formulations. For example, the Smooth Field Approximation could be applied to enable the EMT to account for the concentration difference imposed.[42,54] Further developments have been proposed to modify Methods I and II and enable them to predict the properties of anisotropic networks.[55–58] Implementing these approaches is beyond the scope of this work, which is to quantify the deviations of Methods I and II when applying them to heterogeneous and/or anisotropic pore networks, against the stochastic approach. It should be acknowledged that, in the networks considered here, anisotropic features were introduced by design; in realistic networks it is not always possible to understand whether the pore networks are heterogeneous or anisotropic, because often only 2D visualizations such as those of Fig. 6 are available.[59] Under such circumstances, deciding whether to implement deterministic approaches becomes complex. Because we expect our results to be more likely applicable to practitioners, we implemented Methods I and II in their original formulation, with the understanding that more appropriate deterministic models could be applied to better capture the anisotropy and heterogeneity of the investigated systems.

4.5 Permeability Estimation for a Shale Sample

The insights obtained in terms of the reliability of deterministic and stochastic methods are focused on model problems and well-defined networks; hence, we needed to examine realistic networks and assess the applicability of the three methods to samples of industrial interest, which consist of an organic and inorganic constituent randomly configured. We follow the methodology described in Section 3.4 to obtain the effective organic, inorganic, and matrix permeability.

Fig. 13 shows a sample of the organic (left), inorganic (middle), and matrix networks (right) generated stochastically. The left panel shows the permeability distribution within the organic matter, middle shows permeabilities assigned with the inorganic matter, and right reports a matrix network considered. For the latter dual-permeability network, the red blocks represent organic matter and the light blue ones the inorganic pores.

Table 2 shows the results and the experimental data for the Eagle Ford formation. Note that the experimental permeability strongly depends on the conditions selected (temperature and pressure). Table 3 shows the results of our permeability predictions.

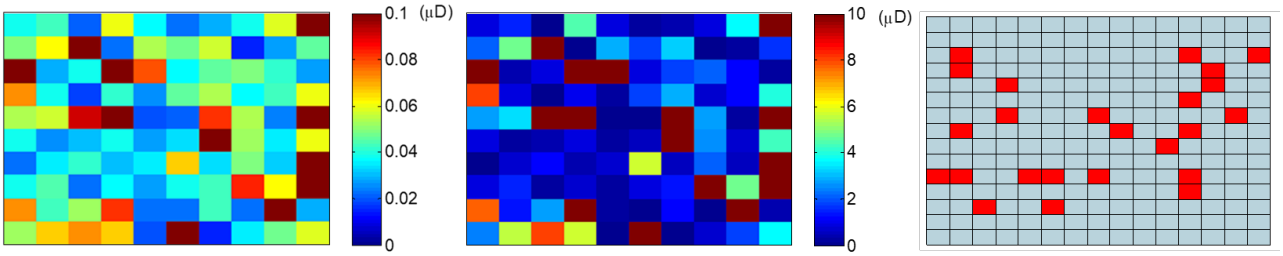

Fig. 13. Example of the permeability distribution within the organic matter (left), permeability distribution of the inorganic matter (middle) and the distribution of organic matter in the inorganic matrix (right). The color bars represent permeability coefficients in μD.

Table 2: Permeability calculation of the organic and inorganic matter, and the effective network permeability using EMT, simplified renormalization and KMC methods. Error bars for matrix permeability calculation for Methods I and II are based on the minimum, maximum and average permeability using Eq. (15). The uncertainty assigned to the KMC calculation represents the confidence interval (99.9%).

Methods	Organic	Inorganic	Matrix
EMT	0.05±0.01 μD	2.5±0.13 μD	1.46±0.03 μD
Simplified renormalization	0.05±0.01 μD	1.43±0.07 μD	0.38±0.02 μD
KMC	0.08±0.02 μD	1.56±0.35 μD	1.11±0.15 μD
Experiments	N/A	N/A	0.1-0.6[60–62] μD

As expected from our previous observations for broad log-normal PSDs (Fig. 8), EMT over-estimated the permeability for the inorganic constituent compared to both Methods II and III. However, for the organic component, all three methods agree, because the PSD is narrow. For the matrix permeability, the EMT predicts the largest permeability, simplified renormalization predicts the smallest, and KMC predicts a value that lies between those from the two deterministic methods.

We compare the matrix permeability predicted against the values reported by Naraghi et al.[27] for the same SEM image. Using Method II with 40 stochastic configurations, those authors predicted the permeability to be 0.28 μD; implementing the same approach, we predict an effective matrix permeability of 0.38 μD. The difference might be because of the slightly higher mean values (μ) assumed in our organic and inorganic PSDs, the reduced number of configurations considered, or the methodology we followed to calculate separately effective organic and inorganic permeability before characterizing the dual-permeability network. However, we consider the two predictions proximate.

Table 3: Permeability calculation of the organic and inorganic matter, and the effective network permeability using EMT, simplified renormalization and KMC methods. The organic matter is the high-permeability component. The uncertainty assigned to the KMC calculation represents the confidence interval (99.9%).

Methods	Organic	Inorganic	Matrix
EMT	2.5±0.13 μD	0.05±0.01 μD	0.29±0.02 μD
Simplified renormalization	1.43±0.07 μD	0.05±0.01 μD	0.15±0.01 μD
KMC	1.56±0.35 μD	0.08±0.02 μD	0.36±0.15 μD
Experiments	N/A	N/A	0.1-0.6 μD [60–62]

More importantly, we compare the predicted matrix permeability against experimental data. While varying the confining stress applied to an Eagle Ford plug sample, Peng and Locks measured permeabilities between 0.1 and 0.6 μD;[61] other experimental studies[60,62] report values within the same range. The effective matrix permeability predicted using Method I was significantly larger than these values (see Table 2), while Method II yielded a reasonable estimate (0.38±0.02 μD). For the networks considered for Fig. 13 (right), the KMC prediction deviated substantially from experimental data and multiple reasons could explain this. For instance, in our model the rock porosity was considered constant (10%) over the 10-network ensemble, while, in reality, this is a variable quantity and is generally less than 10%. We did not account for adsorption phenomena, but only for Knudsen diffusivity. Our analysis is based on a single SEM image, which exhibits low anisotropy. It is possible that the sample used for the experiments was anisotropic, while only an average permeability value was reported.[51] Because the KMC approach is affected by assumptions made about network connectivity and anisotropy, these simplifications might have affected the KMC predictions.

Furthermore, it is possible that the deviation between KMC predictions and experimental data is because of the underlying assumption about the pore networks. So far, we followed the assumption that the narrow pores (1-10 nm) in the shale sample correspond to micropores in organic matter, while the larger pores are those in the inorganic matter. This assumption might not be realistic; actually, recent adsorption studies on clays demonstrate that the inorganic constituent comprises pore sizes of 1 to 10 nm.[63] Loucks et al.[64] reported that organic matter particles generally range between 5 and 75 nm in length. Taking these observations under consideration, we use the permeability coefficients in Table 2, as calculated by the KMC method, and generate networks where the organic matter is the high-permeability component (1.56 μD), and the inorganic matter the low-permeability one (0.08 μD). The effective matrix permeability calculated from 10 independent stochastic simulation runs using 10 different configurations with the KMC method yielded an effective matrix permeability of 0.36 μD with a confidence interval of ±0.15 μD (Table 3). This falls within the experimental range of permeability reported, suggesting that the stochastic KMC approach could be a viable option for predicting permeability of shale rock samples. We expect, however, that 3D representations of the model will be much more reliable. For completeness note that Table 3 shows that Methods I and II also predict permeability values that are consistent with the experimental observations. This is not unexpected, considering that Fig. 6 suggests that the shale sample considered here is rather isotropic. A more stringent discrimination among the three methods could be attained when data for an anisotropic sample are available; this will be performed in the future.

Moreover, our results show that, despite the complexity of the shale sample considered, which contains both organic and inorganic pores, as well as a dual-permeability network, using 10 realizations for the KMC model and assuming that the organic matter is the high-permeability component provides a network permeability with confidence intervals within the experimental range.

5 Conclusions

We performed a thorough comparison between three approaches (two deterministic and one stochastic) to assess their ability to evaluate the permeability of model pore networks. The EMT and simplified renormalization methods were selected, within their original derivations, as deterministic models because of their simplicity. We compared those against our KMC algorithm that has provided useful transport insights for our recent studies restricted to 1D pore networks. We discussed how the KMC method can be implemented for a 2D lattice, requiring reasonable computational resources. We considered pore networks with varying PSDs; dual-permeability networks with different % content of micro-, meso-, and macropores; isotropic and anisotropic configurations; and one realistic network designed to replicate the cross section of a shale rock sample.

Our findings both confirm observations from previous studies and provide new insights. We compared the deterministic results against KMC predictions, considering KMC to provide accurate estimations, and we identified narrow log-normal distributions to be ideal for applying the EMT and the renormalization method. Both deterministic methods were sensitive to small changes in the amount of high-permeability pores rather than changes in the low-permeability ones. For broad distributions, the EMT always overestimated the network's permeability; the simplified renormalization method provided low estimates because of the zero crossflow assumption while the KMC predictions were between the two. For networks with dual permeability, the simplified renormalization method was suitable for cases of spatially uniform systems that had equal parts of the low- and high-permeability components. The EMT was suitable for mesoporous systems containing up to 25% of micro- or macropores without generating anisotropy to the flow direction (spatially uniform systems). For all other cases considered in this study, EMT overestimated the matrix permeability.

Based on our analysis, among the approaches considered, KMC is the most sensitive and reliable method, because it responds to changes in both the low- and high-permeability values. For dual-permeability networks, KMC detected changes proportional to the components and provided an estimate that captured the structural features of the matrix. The most valuable feature of KMC, compared to the deterministic methods considered, is its sensitivity to anisotropy. KMC could be applied to low-connectivity networks and could quantify the effect of small-scale heterogeneities (e.g., local low connectivity). When the KMC was applied to predict the permeability of a shale sample for which one SEM image was available together with data on PSDs, we compared our findings against experiments. Since no experimental data were available corresponding to the shale SEM image, laboratory permeability experiments conducted on Eagle Ford samples were used as reference, yielding a broad range for the experimental permeability range used for comparison. Given the dataset available, using 10 stochastic realizations for the organic, inorganic and dual-permeability networks, was sufficient to yield KMC results in reasonable agreement with experiments, when considering the organic matter to be the highly permeable portion of the matrix. To achieve agreement with a narrower experimental range would require simulating more stochastic realizations of the lattices representing the dual networks, which would yield smaller confidence intervals, at the expense of higher computational resource requirements.

The accuracy of the KMC method can be improved by extending our analysis to more images of a plug sample, so that anisotropy and local heterogeneities are considered, accounting for the effect of adsorption and the true porosity. The disadvantage of KMC, compared to deterministic techniques, rests with the necessary computing time. The deterministic methods provided results in a few seconds, while the computational cost of KMC ranged from minutes to hours. Therefore, a future challenge is to efficiently use the KMC method to analyze permeability of an entire plug sample, while accounting for realistic phenomena such as preferential adsorption.

6 Notation

A = cross-sectional area (m^2)

D_f = fractal dimension of the pore surface

$D_{i,j}$ = diffusion coefficient (m^2/s)

D_k = Knudsen diffusion coefficient in a smooth pore (m^2/s)

D_x = diffusion coefficient on x-direction (m^2/s)

D_{xy} = diffusion coefficient on xy plane (m^2/s)

D_y = diffusion coefficient on y-direction (m^2/s)

g_m = effective conductance (S)

g_x = local conductance (S)

J = molecular flux (mol/m^2s)

k_D = is the Darcy permeability (m^2)

k_{eff} = effective matrix permeability (m^2 or Darcy)

$k_{i,j}$ = permeability coefficient of the voxel located in row i and column j (m^2 or Darcy)

k_{LB} = lower bound permeability (m^2 or Darcy)

Kn = Knudsen number (dimensionless)

k_{UB} = upper bound permeability (m^2 or Darcy)

M = fluid molar mass (g/mol)

N_A = Avogadro number (=6.023×10^{23} atoms/mol)

N_C = total number of columns

N_R = total number of rows

$P_p(t)$ = probability of a particle to enter voxel p (dimensionless)

$P_q(t)$ = probability of a particle to enter voxel q (dimensionless)

r_{KMC} = KMC transition rate (s^{-1})

R = universal gas constant (=8.314 J/g mol·K)

$R_{i,j}$ = pore radius of the voxel located in (i, j) (nm)

T = temperature (K)

W_{pq} = kinetic constant for a transition from voxel p to voxel q

W_{qp} = kinetic constant for a transition from voxel q to voxel p

z = coordination number (dimensionless)

ΔC = concentration difference, C_{top}-C_{bottom} (mol/m^3)

ΔP = pressure difference, P_{top}-P_{bottom} (MPa)

Δt = time step (s)

δ = distance between the centres of two consecutive voxels (nm)

δ' = ratio of normalized molecular size to local average pore diameter

η = fluid viscosity (cP)

θ = porosity (dimensionless)

ρ_{av} = average gas density (kg/m^3)

τ = tortuosity (dimensionless)

$\varphi_{i,j}$ = weighting factor (dimensionless)

PSD = pore size distribution

BET = Brunauer, Emmett, and Teller

Acknowledgements

We thank Halliburton for financial support and acknowledge the use of the UCL Legion High Performance Computing Facility (Legion@UCL) and associated support services for the completion of this work. This research received funding from the European Union's Horizon 2020 research and innovation program under Grant Agreements No. 640979 and No. 764810 and from the Marie Curie Career Integration Grant No. 2013-CIG-631435 to AS.

Appendix A. Supplementary data

Supplementary data to this article can be found online at (DOI required)

References

1. BP Statistical Review of World Energy June 2017. 2017;66th editi(June).
2. Kelkar M. *Natural Gas Production Engineering*. (Patterson M, ed.). Tulsa, Oklahoma: PennWell; 2008.
3. Smith MB, Montgomery CT. *Hydraulic Fracturing*. First. CRC Press; 2015.
4. H.Schön J. Chapter 1 - Rocks—Their Classification and General Properties. In: Schön JH, ed. *Developments in Petroleum Science*. First. Elsevier B.V.; 2015:1-19.
5. Sayed MA, Al-muntasheri GA, Liang F. Development of shale reservoirs : Knowledge gained from developments in North America. *J Pet Sci Eng*. 2017;157(July 2016):164-186.
6. Woods AW. *Flow in Porous Rocks Energy and Environmental Applications*. First. Cambridge, United Kingdom: Cambridge University Press; 2014.
7. Mansfield P, Issa B. Fluid Transport in Porous Rocks . I . EPI Studies and a Stochastic Model of Flow. *J Magn Reson*. 1996;122(Series A):137-148.
8. Saif T, Lin Q, Butcher AR, Bijeljic B, Blunt MJ. Multi-scale multi-dimensional microstructure imaging of oil shale pyrolysis using X-ray micro-tomography , automated ultra-high resolution SEM , MAPS Mineralogy and FIB-SEM. *Appl Energy*. 2017;202:628-647.
9. Ling K, He J, Pei P, Han G, Zhang H. Determining the permeability of tight rock with gas transient flow. *J Nat Gas Sci Eng*. 2013;15(NOVEMBER):1-7.
10. Liu X, Bin YZ, Yu GJ. From molecular dynamics to lattice Boltzmann : a new approach for pore-scale modeling of multi-phase flow. *Pet Sci*. 2015;12:282-292.
11. Dagan G. Models of Groundwater Flow in Statistically Homogeneous Porous Formations.

Water Resour Res. 1979;15(1):47-63.

12. Ph. Renard MG de. Calculating equivalent permeability: a review. *Adv Water Resour*. 1997;20:253-278.

13. Kerner EH, Bailey AC, Waterhouse N, Yates B, Mackenzie JK. The Elastic and Thermo-elastic Properties of Composite Media. *Proc Phys Soc Sect B*. 1956;69:808-813.

14. Bruggeman VDAG. Berechnung verschiedener physikalischer Konstanten von heterogenen Substanzen. *Ann Phys*. 1935;5(24).

15. Landauer R. The Electrical Resistance of Binary Metallic Mixtures. *J Appl Phys*. 1952;23(7):779-784.

16. Kirkpatrick S. Percolation ancl Conduction. *Rev Mod Phys*. 1973;45(4):574-588.

17. Kanellopoulos NK, Petrou JK. Relative gas permeability of capillary with various size distributions networks. *J Memb Sci*. 1988;37:1-12.

18. Davis HT. The Effective Medium Theory of Diffusion in Composite Media. *J Am Ceram Soc*. 1977;60(11-12):499-501.

19. Jiang J, Younis RM. A multimechanistic multicontinuum model for simulating shale gas reservoir with complex fractured system. *Fuel*. 2015;161:333-344.

20. Khatlb ZI, Vitthal S. The Use of the Effective-Medium Theory and a 3D Network Model To Predict Matrix Damage in Sandstone Formations. *Soc Pet Eng J*. 1991;(May):233-239.

21. Daigle H, Screaton EJ. Predicting the permeability of sediments entering subduction zones. *Geophys Res Lett*. 2015;42:5219-5226.

22. Singh T, Kang D, Nair S. Rigorous calculations of permeation in mixed-matrix membranes : Evaluation of interfacial equilibrium effects and permeability-based models. *J Memb Sci*. 2013;448:160-169.

23. Bunde A, Dieterich W. Percolation in Composites. *J Electroceramics*. 2000;5(2):81-92.

24. King PR. The Use of Renormalization for Calculating Effective Permeability. *Transp Porous Media*. 1989;4:37-58.

25. Renard P, Loc'h G Le, Ledoux E, Marsily G De, Mackay R. A fast algorithm for the estimation of equivalent hydraulic conductivity of heterogeneous media. *Water Resour Res*. 2000;36(12):3567-3580.

26. Kelkar M, Perez G. *Applied Geostatistics For Reservoir Characterization*. First. (Chopra A, ed.). Richardson, Texas: Society of Petroleum Engineers Inc.; 2002.

27. Naraghi ME, Javadpour F. A stochastic permeability model for the shale-gas systems. *Int J Coal Geol*. 2015;140:111-124.

28. Metropolis N, Arianna R, Marshall R, Teller A, Teller E. Equation of State Calculations by Fast Computing Machines. *J Chem Phys*. 1953;21(6):1087-1092.

29. Apostolopoulou M, Day R, Hull R, Stamatakis M, Striolo A. A kinetic Monte Carlo approach to study fluid transport in pore networks. *J Chem Phys*. 2017;147(134703):1-10.

30. Dai J, Seider WD, Sinno T. Lattice kinetic Monte Carlo simulations of defect evolution in crystals at elevated temperature. *Mol Simul*. 2006;32(3-4):305-314.

31. Kolokathis PD, Theodorou DN. On solving the master equation in spatially periodic systems On solving the master equation in spatially periodic systems. *J Chem Phys*. 2012;137(34112):1-21.

32. Ma L, Slater T, Dowey PJ, et al. Hierarchical integration of porosity in shales. *Sci Rep*. 2018;8(11683):1-14.

33. Redner S. Fractal and Multifractal Scaling of Electrical Conduction in Random Resistor

Networks. In: Meyers RA, ed. *Mathematics of Complexity and Dynamical Systems*. New York: Springer; 2009:1858.

34. Van Kampen NG. Chapter 5: The Master Equation. In: *Stochastic Processes in Physics and Chemistry*. Elsevier B.V.; 2007:96-133.

35. Stamatakis M, Farmer B, Luskin M, Plechá P. First principles-based kinetic Monte Carlo simulation in catalysis. In: *Physics of Surface, Interface and Cluster Catalysis*. IOP Publishing, Bristol, UK; 2016:38.

36. Gillesple DT. Exact Stochastic Simulation of couple chemical reactions. *J Phys Chem*. 1977;81(25):2340-2361.

37. Matsumoto M, Nishimura T. Dynamic creation of pseudorandom number generators. *Monte Carlo and Quasi-Monte Carlo Methods*. 2000;1(1):56-69.

38. Karayiannis NC, Mavrantzas VG, Theodorou DN. Diffusion of small molecules in disordered media : study of the efect of kinetic and spatial heterogeneities. *Chem Eng Sci*. 2001;56:2789-2801.

39. Gibson MA, Bruck J. Efficient Exact Stochastic Simulation of Chemical Systems with Many Species and Many Channels. *J Phys Chem A*. 2000;104(9):1876-1889.

40. Brown GO. Henry Darcy and the making of a law. *Water Resour Res*. 2002;38(7):1-12.

41. Tyrrel HJ V. The Origin and Present Status of Fick â€™ s Diffusion Law. *J Chem Educ*. 1964;41(7):397-400.

42. V. N. Burganos SVS. Diffusion in Pore Networks : Effective Medium Theory and Smooth Field Approximation. *AIChE J*. 1987;33(10):1678-1689.

43. Coppens M. The effect of fractal surface roughness on diffusion and reaction in porous catalysts – from fundamentals to practical applications. *Catal Today*. 1999;53:225-243.

44. Tsonopoulos C. Critical Constants of Normal Alkanes from Methane to Polyethylene. *AIChE J*. 1987;33(12):2080-2083.

45. Sing KSW, Everett DH, Haul RAW, et al. Reporting Physisorption Data For Gas/Solid Systems with Special Reference to the Determination of Surface Area and Porosity. *Pure Appl Chem*. 1985;57(4):603-619.

46. Sitar N, Cawlfield D, Kiureghian A. First-Order Reliability Approach to Stochastic Analysis of Subsurface Flow and Contaminant Transport. *Water Resour Res*. 1987;23(5).

47. Li Y, Leboeuf E, Basu P., Mahadevan S. Stochastic Modeling of the Permeability of Randomly Generated Porous Media. *Adv Water Resour*. 2005;28(8):835-844.

48. Karacan CÖ, Olea RA. Stochastic reservoir simulation for the modeling of uncertainty in coal seam degasification. *Fuel(Lond)*. 2015;148:87-97.

49. Capek P, Vesely M, Bernauer B, et al. Stochastic reconstruction of mixed-matrix membranes and evaluation of effective permeability. *Comput Mater Sci*. 2014;89:142-156.

50. Wu K, Van Dijke MIJ, Couples GD, et al. 3D stochastic modelling of heterogeneous porous media - Applications to reservoir rocks. *Transp Porous Media*. 2006;65:443-467.

51. Backeberg NR, Iacoviello F, Rittner M, et al. Quantifying the anisotropy and tortuosity of permeable pathways in clay-rich mudstones using models based on X-ray tomography. *Sci Rep*. 2017;(June):1-12.

52. Bui T, Phan A, Cole DR, Striolo A. Transport Mechanism of Guest Methane in Water-Filled Nanopores. *J Phys Chem C*. 2017;121:15675-15686.

53. Ringnér M. What is principal component analysis ? *Nat Biotechnol*. 2008;26(3):303-304.

54. Jörg Kärger, Douglas M. Ruthven DNT. *Diffusion in Nanoporous Materials*. 2nd ed. Wiley-VCH Verlag GmbH & Co. KGa; 2012.

55. Zhang X, Wu Y. Effective medium theory for anisotropic metamaterials. *Sci Rep*. 2015;5(7892):1-7.

56. Cherkaev OL and E. Effective medium approximations for anisotropic composites with arbitrary component orientation. *J Appl Phys*. 2015;114(164102):1-8.

57. Bernasconi J. Conduction in anisotroyic disordered systems: Effective-medium theory. *Phys Rev B*. 1974;9(10):4575-4579.

58. Preux C, Ravalec M Le, Enchéry G. Selecting an Appropriate Upscaled Reservoir Model Based on Connectivity Analysis. *Oil Gas Sci Technol Rev IFP Energies Nouv*. 2016;71(60):1-15.

59. Wehr SD, Shaw JM. A Note on the Misuse of Area Images to Obtain Particle Size Information in Solid-Solid Systems. 2002;41(3):365-372.

60. Tinni A, Fathi E, Agarwal R, Sondergeld C, Akkutlu Y, Rai C. Shale Permeability Measurements on Plugs and Crushed Samples. *Soc Pet Eng J*. 2012;162235(November):1-14.

61. Peng S, Loucks B. Permeability measurements in mudrocks using gas-expansion methods on plug and crushed-rock samples. *Mar Pet Geol*. 2016;73:299-310.

62. Nazari Moghaddam R, Jamiolahmady M. Fluid transport in shale gas reservoirs: Simultaneous effects of stress and slippage on matrix permeability. *Int J Coal Geol*. 2016;163:87-99.

63. Kuila U, Prasad M. Specific surface area and pore-size distribution in clays and shales. *Geophys Prospect*. 2013;61:341-362.

64. Loucks RG, Reed RM, Ruppel SC, Hammes U. Spectrum of pore types and networks in mudrocks and a descriptive classification for matrix-related mudrock pores. *Am Assoc Pet Geol Bull*. 2012;96(6):1071-1098.